JFM PAPERS

Kinematics and dynamics of pitching flexible panels in a quiescent fluid

Parag Deshpande[1],† **and Abhijeet Vishwasrao**[2]

[1]UAV Design and Integration Division, CSIR-National Aerospace Laboratories, Bangalore 560037, India

[2]Defence Institute of Advanced Technology, Department of Aerospace Engineering, Pune 411025, India

An experimental investigation was carried out to understand the kinematics and dynamics of flexible panels having pure pitching motion in a quiescent fluid. Simultaneous measurements of force and angular position of a panel were performed for various panel configurations. A high-speed camera imaging technique was used to find the instantaneous position of the trailing edge. The wake vortex flow was also quantified using the particle image velocimetry technique (PIV). We established a generic correlation between a time-averaged thrust coefficient C_T and an effective flexural stiffness Π of the panel. The results in terms of both time and phase-evolution of hydrodynamic forces and torque are exhibited through the complete kinematics and dynamics of the pitching panels, perhaps for the first time. The elastic deformation of the flexible panel at stroke reversals is found to affect the longitudinal force generation significantly when compared with the rigid panel. We have described many interesting features related to the elastic deformation of the panel. During stroke reversal, the motion of the pitching for the flexible panels reduces when compared to the pitching motion imposed by the forcing function. Reduced panel motion is found to aid thrust generation for a longer time in a cycle for which magnitude is indirectly governed by the flexural stiffness of the panel. The onset of instantaneous thrust and trailing-edge vortex generation is found to match precisely with the spatio-temporal location of the panel inflection. We noted that both the maximum phase lag ϕ and corresponding hydrodynamic torque T_{hyd} are strongly correlated to the panel's effective flexural stiffness Π.

Key words: flow-structure interactions, swimming/flying

† Email address for correspondence: parag@nal.res.in

1. Introduction

The study of heaving, pitching and flapping motion is a subject of interest in many ways. In nature, the undulating motion of body/wings/fins is utilised to generate a force for their locomotion. Each flying or swimming species has a uniqueness in terms of body weight, size, shape and type of undulating motion. However, they have all one common feature, namely, a flexible undulating body part. It has long been recognised that wing flexibility enhances force generation (Combes & Daniel 2001; Wu *et al.* 2011; Sane & Dickinson 2002; Combes & Daniel 2003; Zhao *et al.* 2010). However, there is only a limited understanding of the fluid-structure interaction (FSI) aspect of the problem because the theories and observations made so far are unique to the particular kinematics of each wing system. In a broader sense, both kinematic motion and wing flexibility go hand-in-hand to generate desired locomotion, which leads to the complexity in finding the answer for the question as to how wing flexibility affects force generation. Wing flexibility also adds, as an additional parameter, resonance, where the ratio of forcing undulating frequency to the resonant frequency affects the wing elastic deformation and subsequently the force generation (Ramananarivo, Godoy-Diana & Thiria 2011; Dewey *et al.* 2013; David, Govardhan & Arakeri 2017). Thus kinematics, forcing undulating frequency and wing flexibility are the three factors with which one can have several permutations and combinations to optimise aero-propulsive performance. In addition, it is the same reason for having diversity in birds and swimming animals as pointed by Combes & Daniel (2001). The recent review by Wu *et al.* (2020) and Smits (2019) acknowledged that some of the areas related to oscillating foils require attention. Wu *et al.* (2020) mentioned the complexities in three-dimensional flow that need to be addressed by considering low aspect ratio flexible oscillating foils as these cases follow the natural flyers/swimmers more realistically. Smits (2019) insinuated that because the kinematics of animal locomotion is a combination of pitching and heaving, attention is required to study the combined kinematic motion to achieve high thrust performance.

In general, many of the previous studies on thrust generation have used the undulating motion (pitching or heaving or the combination of both) given either to a two-dimensional rigid symmetric aerofoil with a flexible foil attached at its trailing edge (Heathcote & Gursul 2007; Heathcote, Wang & Gursul 2008; Kang *et al.* 2011; Shinde & Arakeri 2014; David *et al.* 2017), or given directly to the shaft on which a low aspect ratio flexible panel is attached (Dewey *et al.* 2013; Quinn, Lauder & Smits 2014, 2015; Moore 2014). The major focus of these studies was to understand the effect of foil/panel flexibility and the role of resonance on time-averaged thrust performance. Shinde & Arakeri (2014), Heathcote & Gursul (2007) and David *et al.* (2017) also investigated the vortex dynamics in the wake of the flexible foil. Numerical studies by Kang *et al.* (2011) established the correlation between wing-tip deflection and maximum propulsive force by implementing the scaling of the various parameters. They also noted that the condition of peak averaged thrust generation exists close to the foil resonance. In addition, they found that the peak propulsive efficiency improved when the undulating frequency was set close to half of the natural frequency of the wing. David *et al.* (2017) investigated the effect of flexural stiffness of the flexible flap, its length with respect to chord length of the rigid aerofoil on the mean thrust generation and on its propulsive efficiency. They noted that the axial component of the force became dominant when the flexible flap was attached to the rigid aerofoil that caused the enhancement in the thrust compared to the pitching of the rigid aerofoil alone. They further discussed two cases of maximum thrust generation and optimal propulsive efficiency corresponding to a simple bending mode of a moderately

flexible flap and higher mode of deformation of a highly flexible flap, respectively. Shinde & Arakeri (2014) found a strong influence of flexibility of a pitching foil on a jet meandering in a quiescent fluid condition. Their findings revealed that the foil flexibility restricted the jet meandering, which in turn improved the time-averaged thrust generation. Quinn *et al.* (2015) demonstrated experimental optimisation to maximise the propulsive efficiency of a flexible panel having both heave and pitch motion with a forward flow condition. Parameters such as Strouhal number, actuation frequency, phase lag between pitch and heave motions have been optimised and achieved an efficiency of approximately 0.38 for the combined pitch and heave motions, which is nearly double the highest efficiency obtained for heave motion only. They used linear beam theory to obtain the resonant frequency of the fluid-structure system. Zhu *et al.* (2017) discussed the propulsion performance of the tuna fish through bio-inspired flexible panels having combined pitching and heaving motion. They observed that chordwise flexible panels improved swimming performance as compared to rigid panels. Lauder *et al.* (2007) analysed the experimental data of kinematics and hydrodynamics of real fish and developed a robotic fish model to investigate the effect of flexibility on propulsive performance.

It is surprising to note that all these investigations are based on the time-averaged thrust generation, and comparatively less attention was given to the understanding of the mechanism of instantaneous thrust generation owing to the undulating motion of the flexible foil/panel, despite the highly unsteady nature of the problem. The instantaneous force generation and its variation are directly linked with the wing kinematics. We find that the instantaneous force analysis was done only for the configurations having more complex kinematics. Sane & Dickinson (2002) studied the instantaneous force variation owing to a rigid mechanical wing resembling an insect wing, having rotational motion in all three planes. Shkarayev & Rajeev (2014) found the instantaneous force variation of an actual locust wing. However, it is difficult to understand the generation of instantaneous forces because of the complex kinematics discussed in these investigations. Numerical investigations by Vanella *et al.* (2009) showed that progressive elastic deformation of a flexible wing during stroke reversal produces stronger leading-edge and trailing-edge vortices (LEV and TEV, respectively) than that of a rigid wing. They compared various frequency ratios of wingbeat frequency to the resonant frequency of the wings. They observed very high elastic deformation for a very low-frequency ratio that caused a negative effect on the aerodynamic force generation. Massey, Flick & Jadhav (2009) demonstrated the instantaneous force variation in a flapping cycle for a flexible wing and showed that with an increase in wing stiffness there is a significant improvement in lift generation. Coleman *et al.* (2018) showed a strong correlation between instantaneous force and wing deformation for a flexible flapping wing in hover conditions. Ramananarivo *et al.* (2011) pointed out the elastic deformation of the trailing edge of a flexible wing during stroke reversal. In their experimental study, they discussed a phase lag between wing motion and trailing edge owing to flexibility. They further noted that for optimal performance, maintaining optimal phase lag is very important, and depends on the wing flexibility. Ramananarivo, Godoy-Diana & Thiria (2012) developed a theoretical model to mimic anguilliform swimmers based on simple beam theory and Lighthill's potential flow model for undulatory propulsion. They predicted the kinematics and propulsive forces with better accuracy, because the deformation of the body was dominated by the elastic properties rather than the fluid-dynamic forces. The phase-lag variation between pitching and heaving motions is an important parameter in determining the propulsive efficiency (Anderson *et al.* 1998; Zhang, Liu & Lu 2010). Anderson *et al.* (1998) pointed

out that thrust performance is critically dependent on the phase lag (75° for highest thrust efficiency) between pitch and heave motion as it critical in the timing of the formation and shedding of LEV, that then interact with the TEV to produce a reverse Kármán vortex street. Zhang *et al.* (2010) simulated heaving and passive pitching dynamics for a flexible two-dimensional flat plate. They noted that the phase lag is in the range 60–90°. Heathcote & Gursul (2007) and Heathcote *et al.* (2008) performed an investigation on instantaneous trailing-edge deflection and phase lag for both chordwise and spanwise flexible aerofoil configurations having a pure heave motion, respectively. In their studies, the shape of the elastic deformation of the aerofoil was represented by pitch angle, pitch phase lag and amplitude of trailing-edge deflection. They correlated the foil stiffness characterised by these three parameters against the time-averaged thrust. However, there is a need to understand the effect of flexural stiffness on instantaneous thrust generation.

In the present study, a pitching motion has been applied to the leading edge of the low aspect ratio flexible panels in a quiescent fluid. The rotation of the panel about its fixed leading edge resembles the motion of the tail fin of a fish. Unlike previous studies by Smits' group (Buchholz & Smits 2008; Green & Smits 2008; Dewey *et al.* 2013), we control the flexural stiffness by varying both chord length and span such that the panel area remains constant, in order that we can better investigate its effect on instantaneous force generation. We examine the effect of flexibility on the kinematics and dynamics of the panels based on unsteady force measurements, high-speed imaging techniques and particle image velocimetry (PIV) measurements. This investigation helps improve the understanding of the role of wing flexibility on instantaneous thrust generation and assist in maximising the thrust performance of a flexible panel.

2. Experimental set-up

The experimental set-up consisted of a hollow carbon-fibre shaft of length 0.5 m and diameter 11 mm coupled to a high-torque brushless digital servo (HiTech HS7954SH) to generate a sinusoidal pitching motion. The servo was clamped upside down on Linos X-profile rail assembly below which a square toughened glass tank (0.57 m × 0.57 m × 0.39 m), filled with water, was housed on a 4 in. thick foam sheet as shown in figure 1. The shaft was held vertically in the tank and supported by a ball-bearing mounted within a 5 mm thick acrylic plate clamped horizontally to the rail below the servo assembly. A large size binder clip used for clamping the panels was screwed to the shaft. Two acrylic plates of 2 mm thickness, 7 mm width and 100 mm length were glued to the clamping surface of the binder clip using a hardener. Two asbestos strips, glued to the surface of the acrylic plates, served as fixtures in order to tightly clamp the various panel configurations. A slider was used to move the shaft in the vertical direction to adjust the position of the panel. The panel position was maintained at a sufficient height from the tank bottom to avoid wall effects.

Four low aspect ratio rectangular panels were considered in the present study, having thicknesses of 2 mm (Panel A), 0.77 mm (Panel B), 0.5 mm (Panel C) and 0.125 mm (Panel D). Each panel was classified further by changing its aspect ratio (AR) to do this its chord (c) and span (b) were varied such that the surface area (A) for all the panel configurations was kept constant ($A = 3240$ mm^2). Panel A was divided into four aspect ratios as A_3, A_8, A_9 and A_{10}. Panel B was divided into nine aspect ratios as $B_{1-6,8-10}$, C and D were similarly divided into ten aspect ratios. Table 1 summarises the panel configurations based on their material, thickness, chord and span dimensions. The purpose
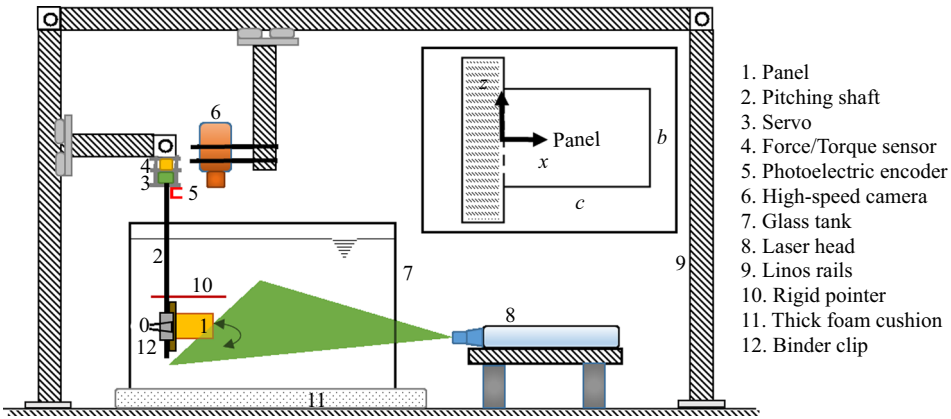
Figure 1. Schematic of the experimental set-up. An inset shows detailed geometry of the panel. The hatched 'T' portion shown is the clamping surface to held the panel firmly to the pitching shaft.

Panel Configuration			Panel A			Panel B	Panel C	Panel D		
Material			Acrylic			PEI	PET	Polyester flim		
Thickness (t), mm			2			0.77	0.5	0.125		
Young's modulus (E), GPa			3			2.95	3.45	3.25		
Panel numbering	1	2	3	4	5	6	7	8	9	10
Aspect ratio	0.44	0.5	0.625	0.9	1	1.1	1.3	1.6	1.85	2
Chord length, mm	85	80	72	60	57	54	50	45	42	40
Span, mm	38	40	45	54	57	60	65	72	78	80

Table 1. Compilation of the panel configurations based their geometrical specifications and elastic properties. The panel configurations are defined by writing a number corresponding to an aspect ratio as a subscript to the panel name.

of aspect ratio variation was to vary the panel flexural stiffness (EI), considering the panel as a cantilever beam. We generated a wide variety of flexural stiffness values by changing the aspect ratio of the four panels. In the previous studies by Buchholz & Smits (2008), the chord length of the panels was kept constant and the span was varied to change the aspect ratio, However, that also resulted in a variation of the panel surface area. A typical 'T' shaped extension to the panel shown in an inset of figure 1 was provided to clamp the panel to the shaft so that the effective area and chord length remained unaltered for each individual panel configuration.

A pure pitching motion, provided as a cosine function $\theta_{LE} = \theta_m \cos(2\pi ft + \pi)$ was applied to the servo by an Arduino board (ATMega 2560). All the experiments were performed at a constant frequency f and amplitude θ_m of 3 Hz and ±20°, respectively. A photoelectric speed encoder (SKU: 6291709189) consisting of a light-emitting diode and receiver was used to monitor the instantaneous position of the shaft. A disc having a single thin slit fabricated using an in-house three-dimensional printing facility was stuck to the shaft to generate two 5 V pulses from the encoder per pitching cycle. The first-mode natural frequency (f_1) for all panel configurations was computed using the equation $f_1 = \alpha \sqrt{EI/\rho_f c^5}$, where α is taken 0.0211 as in David *et al.* (2017). We found

that for the present panel configurations, the ratio of forcing frequency and first-mode frequency (f/f_1) was significantly above 1, and therefore. we did not consider the effect of resonance.

A six-component force/torque sensor (ATI Inc. Mini 40) was used to measure the forces and torque experienced by the panel during pitching motion in stagnant water. The sensor was mounted upside down and sandwiched between the two horizontal acrylic plates, where the plate on the sensor end was firmly screwed to the servo base, and the other acrylic plate was screwed to the slider on the rail. The sensor, servo and shaft were aligned along their longitudinal axes. The transfer of forces and torques from the shaft to the sensor was achieved through four studs holding the two acrylic plates above and below the servo as shown in the schematic depicted in figure 1. Data were acquired at a sampling rate of 3000 Hz, and filtered using an 18 Hz low-pass filter using MATLAB. A total of 30 pitching cycles were considered for time-averaging the forces and torques. A multi-function DAQ device (I/O NI-USB-6210) along with LabVIEW were used to acquire data from the F/T sensor and the photoelectric encoder simultaneously.

A high-speed camera (Phantom 4 M) focused from the top (see figure 1) was used to capture the dynamic chordwise deflection for selected panel configurations ($A_{3,8}$, $B_{1,3,6,8}$, $C_{1,3,6,8}$ and $D_{3,8}$). A thin rigid mild-steel rod was attached radially to the shaft above the binder clip and parallel to the panel chord as shown in figure 1. The rod was used as a reference pointer while measuring the instantaneous angle of the leading edge and deflection of the trailing edge of the panels using high-speed camera images. The frame rate of the high-speed camera was set at 480 fps so that the deformation of the panel could be measured for every $0.5°$ of the leading edge of the panel. The mean standard deviation in the force data obtained from the four data sets was found to be ±10 mN, giving approximately 1 % uncertainty in the mean force data.

PIV was used to measure the flow field in a fixed horizontal plane passing through the midspan of the panel for the selected panel configurations (A_3, B_3, C_3 and D_3). A 65 mJ, 15 Hz dual pulse dual cavity ND-YAG Laser with 532.5 nm wavelength (Litron Inc. nano 65) along with the cylindrical optics was used to illuminate the measurement plane. The Laser was triggered externally through a 5 V pulse generated in the form of a sine function coded on the separate Arduino (ATMega 2560) board. A total of 500 images were captured and the phase averaging was performed in the offline mode only for the selected phases. TSI Inc. Insight 4G software was used to acquire and process the PIV data. A 32×32 interrogation window with 50 % overlap was used in data processing which generated velocity vectors spaced 2.3 mm apart in a 181.5 mm $\times$ 114 mm field of view.

3. Results and discussion

In the absence of freestream velocity (U_∞), time-averaged thrust (T) is normalised by the maximum tangential velocity ($U_t = 2\pi fc$) as given in equation (3.1).

$$C_T = \frac{T}{0.5\rho_f U_t^2 bc} \tag{3.1}$$

Figure 2(*a*) shows the variation of mean coefficient of thrust (C_T) as a function of aspect ratio, for all four panels. Clearly, C_T shows a monotonic increase with an increase in the aspect ratio. Buchholz & Smits (2008) also observed an increase in C_T with aspect ratio at a given Strouhal number for various rigid panel configurations. Unlike Buchholz & Smits (2008) we are solely examining the effect of variation in aspect ratio for the constant

922 A13-6
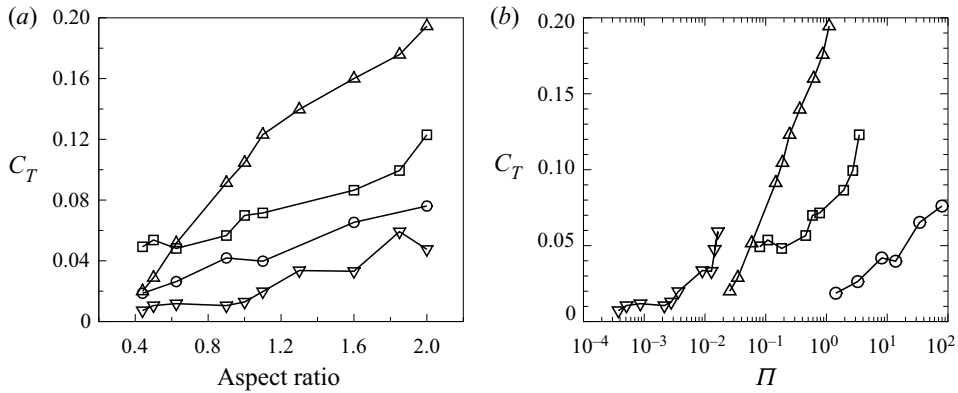
Figure 2. Coefficient of mean thrust as a function of (*a*) aspect ratio (*b*) effective flexural stiffness. ○, panel A; □, panel B; △, panel C; ▽, panel D.

surface area of the panel. Thus the mean C_T is found to increase with a decrease in the panel chord length. Interestingly, Deshpande & Modani (2019) noted the trend of increased C_T with an increase in flapping frequency f for moderately flexible wing configurations. Thus the effect of an increase in frequency f or a decrease in chord c is seen to be the same, because the tangential velocity U_t is a function of both the chord and frequency $f(fc)$.

As described previously, we used panels of various thicknesses (variation in the Young's modulus is only minimal for the panels given in table 1) and also considered various aspect ratios in order to modify the flexural stiffness of the panels. We obtained an effective flexural stiffness (Π) of the panels based on the definition of a non-dimensional flexural stiffness parameter proposed by Kang *et al.* (2011), given in equation (3.2). Owing to the quiescent fluid, we have used U_t instead of U_∞, hence

$$\Pi = \frac{Et^3}{12(1 - \nu_p^2)\rho_f U_t^2 c^3},\tag{3.2}$$

where E and ν_p are Young's modulus and Poisson's ratio of the panel material, respectively. Owing to the combination of thickness and aspect ratio, we obtained a wide spectrum of uniformly spaced effective flexural stiffness Π (35 Πs) ranging from a very low value of $O(-4)$ for Panel D to a very high value of $O(2)$ for panel A. The variation in mean C_T is plotted as a function of Π as depicted in figure 2(*b*). Figure 2(*b*) shows the general trend of increase in C_T with an increase in Π for each panel. The C_T data points were rearranged based on aspect ratio and the effect of aspect ratio was eliminated by dividing both C_T and Π by a corresponding aspect ratio and C_{TAR}; Π_{AR} were obtained. We plot C_{TAR} as a function of Π_{AR}, as depicted in figure 3. The good collapse of C_{TAR} data points can be seen for the entire range of Π_{AR}. It can be seen that C_{TAR} is more sensitive to Π_{AR} in the range $\Pi_{AR} = 0.05$ to 2. For Π_{AR} below 0.05, thrust generation is very low owing to the high flexibility of the panel configurations. For Π_{AR} above 2, C_{TAR} remains nearly constant, indicating that the thrust generation has become independent of the flexural stiffness. We find that various investigators have used flexural stiffness in numerous ways to understand its role in influencing the thrust performance. Kang *et al.* (2011) used effective stiffness in scaling the aerodynamic performance in terms of the normal force acting on the wing causing the wing deformation. David *et al.* (2017) linked a non-dimensional stiffness parameter with the ratio of undulating frequency to the
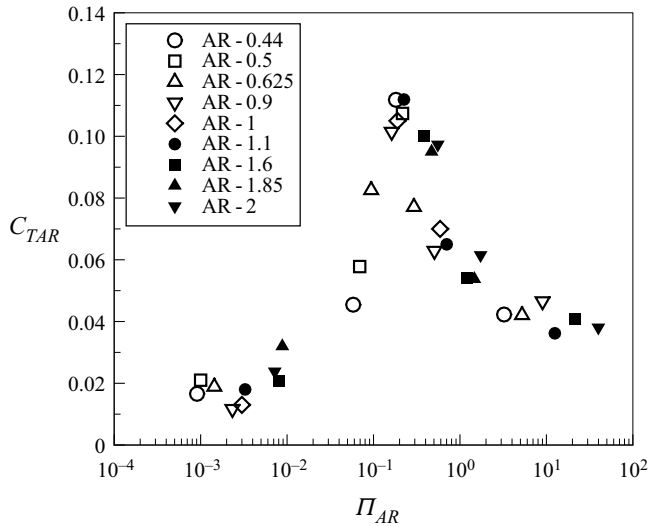
Figure 3. Coefficient of mean thrust as a function of effective flexural stiffness for all the panel configurations having various aspect ratios.

first-mode natural frequency of the foil. Similarly, Dewey *et al.* (2013) showed the collapse of C_T data after scaling the thrust force with the elastic force instead of fluid dynamic force. Compared to the previous findings, we have proposed a straightforward generic correlation between C_T and Π as depicted in figure 3. The trend between C_{TAR} and Π_{AR} suggests that the optimal effective stiffness falls within the range 0.05 to 2. From an engineering point of view, this correlation would be helpful in selecting the various parameters in the Π term (equation (3.2)) to maximise the thrust generation while developing a hovering robotic propulsor for various underwater applications. To have better insight into the role of flexural stiffness on instantaneous thrust generation, we discuss first the kinematics and then the dynamics of the pure pitching cycle in the following sections.

3.1. *Kinematics of the pitching*

Figure 4 shows a typical sequence of high-speed images for the half-cycle for a moderately flexible panel C_3 (see supplementary movie: Panel C_3 available at https://doi.org/10.1017/jfm.2021.494). The thin rigid pointer in these images has improved the visualisation of the actual motion of the panels and has also helped to have a one-to-one comparison of the elastic deformation of the panels against the rigid panel. The angular position of the rigid pointer was used to obtain the leading-edge angle (θ_{LE}) in various panel configurations. In figure 4(*a*), at the onset of the stroke, the pointer is at extreme left and is about to pitch anti-clockwise. Owing to its flexibility, the panel is lagging (pitching clockwise) behind the pointer and has a simple bending deflection (trailing edge bent towards the right). In subsequent instances (figure 4*b*,*c*) we can see that the panel curvature is reducing and it becomes straight where both panel and pointer have reached the same angular position. The spatio-temporal location of this cross-over is nothing but the inflection of the panel for a moderately flexible configurations (see figure 4*c*). After the cross-over, the panel starts to bend on the opposite side (trailing edge bent towards the left) as depicted in figures 4(*d*) to 4(*f*). As the leading edge of the panel (pointer) continues to move anti-clockwise, the panel continues to bend towards the left until it loses its speed and stops completely.
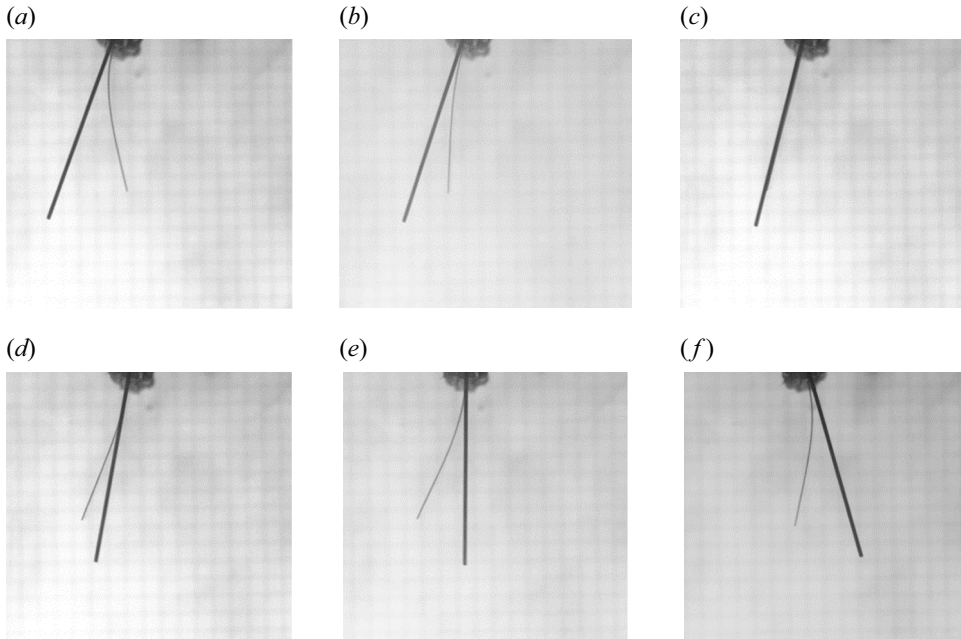
Figure 4. Half-pitching cycle for panel C_3 illustrated by six different phases. (*a*) The rigid pointer is at the extreme left and about to begin an anti-clockwise motion and the panel is lagging behind the pointer and still completing a clockwise motion owing to the flexibility effect. (*b*) Both the pointer and panel are moving towards each other and the phase lag between them is reducing. (*c*) Panel inflection phase, where the pointer and the panel cross each other. (*d*) The panel reaches the extreme left and is about to start an anti-clockwise motion. (*e*) Both the pointer and panel have an anti-clockwise motion, and the phase lag continues to rise from $0°$ at the panel inflection phase to its peak. (*f*) The pointer has reached the extreme right of the stroke and is about to begin the second half of the pitching cycle.

The deceleration of the panel depends on fluid resistance, panel inertia and its elastic properties. In a direct numerical simulation Vanella *et al.* (2009) showed that soon after maximum elastic deformation, there is a release of elastic energy which restores the wing to its undeformed state. They used a torsional spring between two wings, having harmonic motion. Interestingly, we note that when the panel starts to move anti-clockwise, it doesn't evolve to the undeformed condition until it approaches another inflection before the right extreme of the stroke. Thus, except for two inflection states, the panel always remained deformed in a cycle. We also estimated the extent of the trailing-edge deflection as δ_h (before the panel starts to rotate anti-clockwise) as the lateral gap between the trailing edge and pointer, with respect to the panel inflection. The deflection δ_h is found to be $\approx 0.05c$ for both panel B_3 and C_3, with reference to the panel inflection. It is also essential to understand the time-evolution of the elastic deformation of the panel in order to appreciate its effect on the generation of instantaneous forces.

To understand the time-evolution of the elastic deformation of the panel, the sequence of high-speed images was used to obtain the instantaneous angular positions of leading-edge (θ_{LE}) and trailing-edge (θ_{TE}) for the various panel configurations. Heathcote & Gursul (2007) and Ramananarivo *et al.* (2011) had used a similar technique to measure the position of a two-dimensional flexible foil having a pure plunging motion and wings of bird-like flapping model, respectively. In the present case, in every frame, X and Y coordinates at three locations, one at the leading edge, a second at the trailing edge and a third on
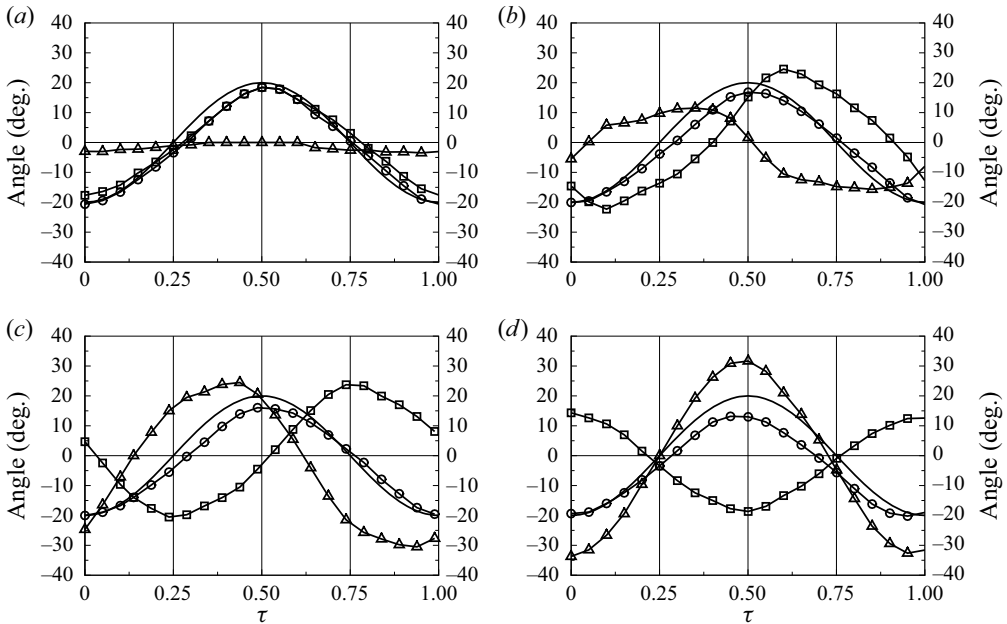
Figure 5. Kinematics of the pitching cycle. Instantaneous angular position of the cosine forcing function of the pitching motion, solid line; instantaneous angular positions of leading edge, ○; trailing edge: □ and phase lag, △ for (*a*) panel A_3 ($\Pi = 3.27$) (*b*) panel B_3 ($\Pi = 0.18$) (*c*) panel C_3 ($\Pi = 0.06$) (*d*) panel D_3 ($\Pi = 0.001$) having same aspect ratio of 0.625.

the pointer having the same *X* coordinate as that of trailing edge of the panel, were measured manually. Trigonometric functions were used to deduce the required angles. Figures 5(*a*) to 5(*d*) show the instantaneous θ_{LE} and θ_{TE} for panel configurations A_3, B_3, C_3 and D_3, respectively as a function of normalised cycle time (τ). The cosine function as an input (θ_{LE}) to the servo and the phase lag ϕ between θ_{LE} and θ_{TE} is also shown in all the plots depicted in figure 5. We observed the deviation in the measured amplitude (θ_{LE}) against the theoretical amplitude (θ_{LE}) obtained from the cosine function. During experiments, we found that the pitching starts from $-20°$, however, the panel doesn't reach $+20°$ (right extreme of the stroke) for most of the panel configurations. The minimum deviation of $4°$ and the maximum deviation of $8°$ are observed for panel C_3 and panel D_3 respectively as depicted in figure 5. The least variation ($<2°$) is observed for panel A (figure 5*a*). The actual pitching frequency, however, was found to be the same as the input frequency of $f = 3$ Hz assigned to the servo. Therefore, we used a constant $1/f = 0.333$ s to normalise the cycle time for all panel configurations. We realised this variation in the stroke amplitude only after analysing the high-speed images. This inconsistency might be because of the servo torque limitations and also to the uncertainty in angle determination from the high-speed images. Because we knew the actual real-time position of the leading edge we took this inconsistency into consideration while analysing the effect of varied flexibility on the instantaneous force generation. In addition, hereafter all the results will be discussed based on observations made on the half-pitching cycle between $\tau = 0$ to 0.5, for simplicity.

The time-evolution of θ_{LE} and θ_{TE} for rigid panel A_3 is depicted in figure 5(*a*) and shows nominal lag (almost no lag) of $\phi < 3°$ towards the left extreme of the stroke. Whereas, the

922 A13-10

time-evolution of θ_{LE} and θ_{TE} for flexible panels shows not only the distinct phase lag between the leading and trailing edges of the panel, but also the trailing-edge motion profile is seen to be entirely different than that of the cosine forcing function. Figures 5(*b*) to 5(*d*) show that the acceleration/deceleration of the trailing edge during the pitching is completely influenced by the panel flexibility. The results from Ramananarivo *et al.* (2011, figure 3*b*) depict broadening of the peak in the instantaneous position data of the trailing edge in comparison with the forcing motion given to the leading edge of the wing. Apparently, in the present case the panel flexibility seems to reduce the motion of the panel especially at the stroke reversals ($\tau = 0$, 0.5 and 1) owing to elastic deformation of the panel. Thus the rudimentary difference between the rigid and flexible panel pitching is, in the former case, time for acceleration/deceleration within a cycle is equal to the forcing function assigned to the pitching shaft. Whereas, in the latter case, owing to elastic deformation, the acceleration/deceleration time in a cycle adjusts itself depending upon the elastic properties of the panel. With an increase in the panel flexibility from panel A_3 to D_3, peak ϕ was found to increase progressively and has a unique trend for each panel configuration (figures 5*b* to 5*d*). The position $\phi = 0$ denotes the panel inflection where both panels and pointer have reached the same angular position. However, it is true only for flexible panels B and C. From the high-speed images, we observed that the panel D_3 did not go under inflection at $\phi = 0$ owing to a higher-order deflection. In addition, for panel D_3, the trailing-edge motion profile is seen to be nearly out of phase as compared with the leading-edge motion profile as depicted in figure 5(*d*).

We find the spatio-temporal location (θ_{LE}, τ) of $\phi = 0$ is an important parameter that is directly linked to the panel flexibility. We noted that with a decrease in the stiffness of the panel, the peak ϕ has increased and the spatio-temporal location of $\phi = 0$ has moved towards the extreme ends of the stroke (figures 5*b* and 5*c*). For panel B_3 the spatio-temporal location of $\phi = 0$ is found to be $\theta = -5°$ and $\tau = 0.05$ very close to the left extreme of the stroke. Whereas, for panel C_3 it is found to be $\theta = -14°$ and $\tau = 0.14$ away from the left extreme. After attaining the peak, ϕ once again, reduces to zero when the panel approaches the other end of the stroke (right extreme). Thus during the time between $\phi = 0$ to its peak ($\phi = \phi_{max}$), we can say that the strain energy is getting stored in the panel during its deformation. The release of the strain energy is taking place when ϕ reduces from ϕ_{max} to 0. Figure 6 shows the time required for storing and releasing the strain energy during winding and unwinding of the panel, respectively. Apparently, the time required to deform the panel from its inflection is more than that required to bring it back to an undeformed state. As much as 70 % of the cycle time is being utilised for storing the energy for panel C_6. It is indeed interesting to see the consequence of $\phi = 0$ (panel inflection) and ϕ_{max} on the instantaneous longitudinal (F_x), lateral force (F_y) and hydrodynamic torque (T_{hyd}) generation, which is discussed in the next section on the dynamics of the pitching.

3.2. *Dynamics of the pitching*

The variation in the longitudinal (F_x, along the *x*-axis) and lateral forces (F_y, along the *y*-axis) with τ for a single-cycle is compared with the corresponding phase-averaged data over ten cycles for panel B_3 is shown in figures 7(*a*) and 7(*b*). The small variation between the single-cycle data and the phase-averaged data shows that the pitching cycles have good repeatability. Therefore, we considered the single-cycle data for all panel configurations in the subsequent discussion. Figures 8(*a*) to 8(*d*) show the time-evolution of the longitudinal and lateral forces plotted along with the angular position of the trailing-edge (θ_{TE}) and the phase lag (ϕ) for panels A_3, B_3, C_3 and D_3 respectively.
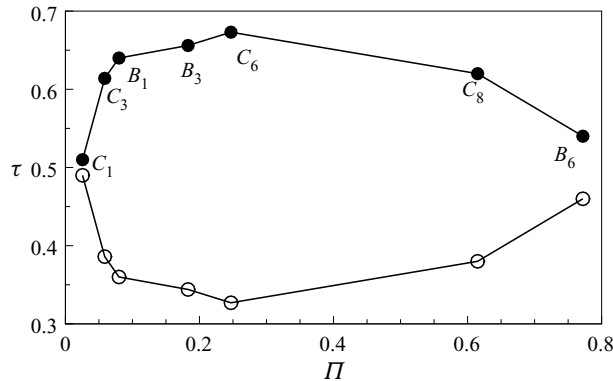
Figure 6. Time required for storing (filled symbols) and releasing (empty symbols) of strain energy for various panel configurations.
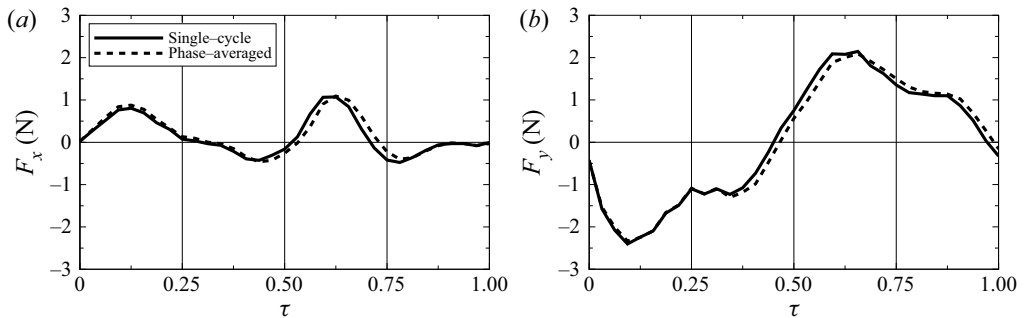

Figure 7. Comparison of the single-cycle data with the phase-averaged data for (*a*) longitudinal force (F_x) and (*b*) lateral force (F_y) force for panel B_3.

In general, at the onset of the cycle, the panel imparts high momentum to the fluid and experiences a strong lateral force F_y as a reaction to it. The lateral force acting on the panel results in its deformation, which depends on the flexibility. The rigid panel does not get deformed and the extent of deformation for a flexible panel depends on its flexural stiffness. Figure 8(*a*) shows that for panel A_3, at the beginning of the stroke ($\tau = 0$ and 0.5), both longitudinal and lateral forces are at their respective peak, and as the cycle progresses these forces reduce to zero at approximately the middle of the stroke ($\tau = 0.25$ and 0.85). This means that there is a generation of both longitudinal and lateral forces during the stroke reversals which corroborates well with the findings from the previous studies (e.g. Sane & Dickinson 2002). The asymmetry in the variation of both F_x and F_y in two half-cycles (see figure 8a) is attributed to the asymmetry in the pitching amplitudes in the two half-cycles described in the previous section. The dynamics of pitching for the flexible panel configurations differs significantly as compared with rigid panel A_3 (see figures 8b to 8d). There is a progressive shift in the inception of F_x and F_y away from the onset of the stroke on a non-dimensional time axis τ. It can be seen that the F_x has started to build up at the spatio-temporal location where the phase lag is zero (see figures 8b and 8d). Thus, flexibility helps in generating additional thrust even before the commencement of the actual stroke reversal. The force F_x attains the peak when the panel trailing edge reaches the stroke extreme $\theta_{TE} = \theta_{TEmax}$ and subsequently F_x reduces to zero prior to the spatio-temporal location where ϕ becomes ϕ_{max}. This is the common trend of
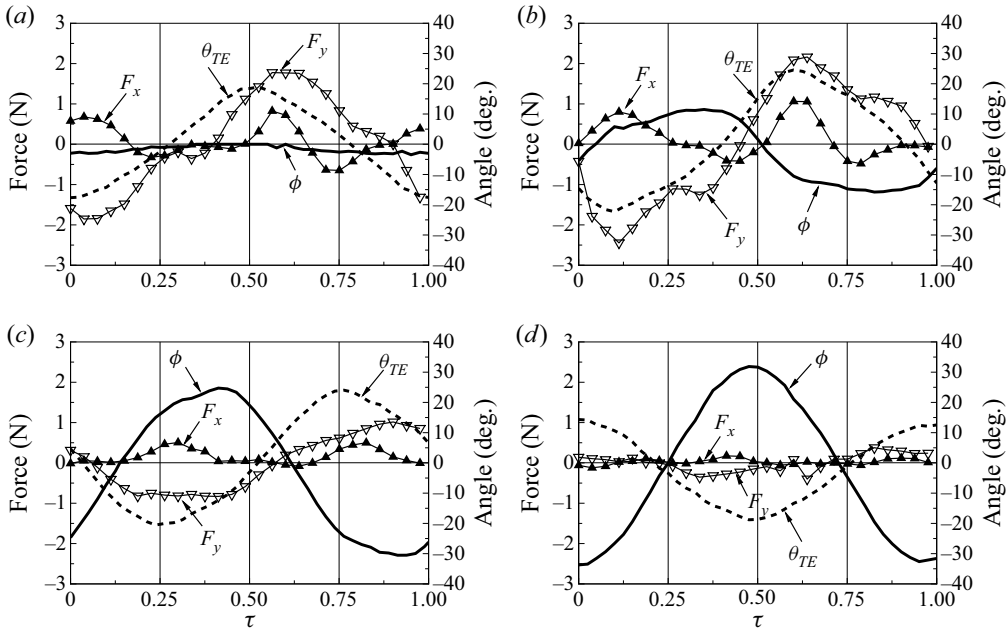
922 A13-12

Figure 8. Instantaneous forces, angular position of the leading edge and phase lag between the leading edge and trailing edge of the panel plotted against a non-dimensional cycle time. Longitudinal force (F_x), ▲; lateral force (F_y), ▽; phase lag (ϕ), solid line; TE angle, dashed line; for (*a*) panel A_3 ($\Pi = 3.27$) (*b*) panel B_3 ($\Pi = 0.18$) (*c*) panel C_3 ($\Pi = 0.06$) (*d*) panel D_3 ($\Pi = 0.001$) having same aspect ratio of 0.625.

the variation in F_x and F_y observed for flexible panel B_3 and panel C_3. As discussed in the previous section, the spatio-temporal locations of θ_{TEmax}, $\phi = 0$ and ϕ_{max}, however, are different for panel B_3 and panel C_3 and seem to be strongly dependent on their respective flexural stiffness. There is also generation of a negative longitudinal force (drag) observed in the second half-cycle ($\tau = 0.74$) for panel A_3. A similar negative peak can be seen from the time-history of C_T by Heathcote *et al.* (2008, figure 6) for a rigid wing. Heathcote *et al.* (2008) mentioned that by introducing spanwise flexibility to the wing, C_T remained positive throughout the heaving cycle. In the present study, it is found that with an increasing order of flexibility from panel B_3 to D_3, the instantaneous longitudinal force remained positive during the entire pitching cycle, as depicted in figures 8(*b*) to 8(*d*). The generation of F_x and F_y forces for a highly flexible panel D_3 were found to be insignificant, and the observation is in line with the result from Kang *et al.* (2011) and Wu *et al.* (2011). Owing to high flexibility, panel D_3 could not produce any reaction force and offered no resistance to the deformation that subsequently caused the higher-order deformation. In general, the magnitude of peak lateral force F_y shows a stronger correlation with the panel flexural stiffness than with the longitudinal force F_x. The trend of F_y variation in figures 8(*a*) to 8(*d*) shows that just before the inflection ($\phi = 0$), F_y changes its sign.

Marais, Wesfreid & Godoy-Diana (2012) have shown that the increase in the thrust force is becaus of an increase in the amplitude owing to foil deformation. From the present study, it is found that along with amplitude increase, the effective time for which the panel generates thrust is equally important. For example, for panel C_3, F_x remained positive for approximately 55 % of the cycle time. Whereas for panel A_3, F_x remained positive only for approximately 44 % of the cycle time, additionally, F_x also remained negative
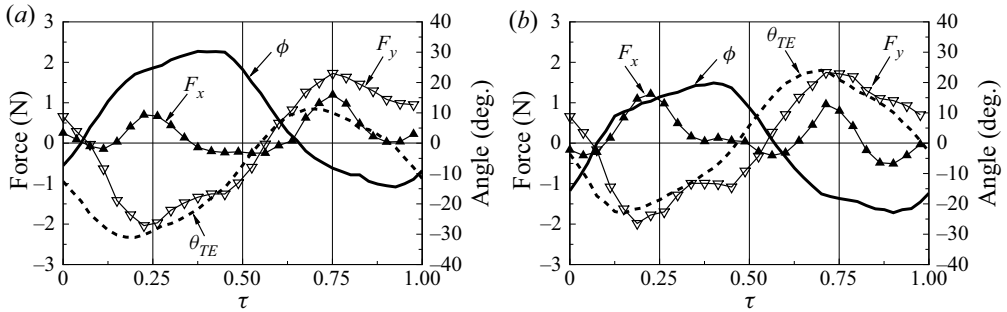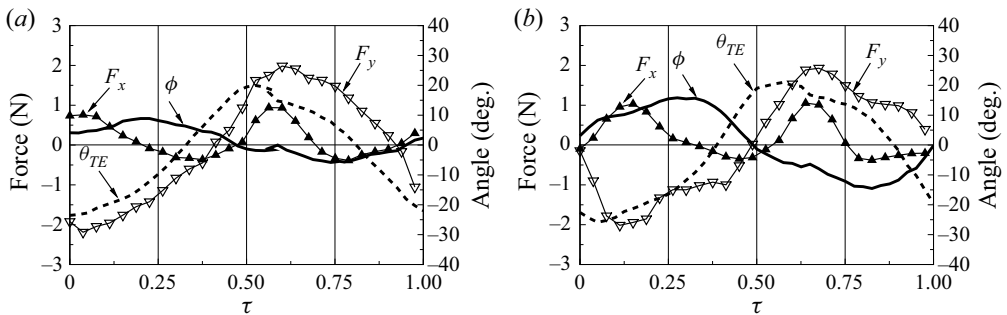
Figure 9. Instantaneous forces, angular position of the leading edge and phase lag between the leading edge and trailing edge of the panel plotted against a non-dimensional cycle time. Longitudinal force (F_x), ▲; lateral force (F_y), ▽; phase lag (ϕ), solid line; TE angle, dashed line; for (a) panel B_1 ($\Pi = 0.08$) (b) panel C_6 ($\Pi = 0.25$) having aspect ratio of 0.44 and 1.1, respectively.

Figure 10. Instantaneous forces, angular position of the leading edge and phase lag between the leading edge and trailing edge of the panel plotted against a non-dimensional cycle time. Longitudinal force (F_x), ▲; lateral force (F_y); ▽; phase lag (ϕ), solid line; TE angle, dashed line; for (a) panel B_6 ($\Pi = 0.77$) (b) panel C_8 ($\Pi = 0.62$) having aspect ratio of 1.1 and 1.6, respectively.

for approximately 36 % of the cycle time, because of which, the mean C_T for panel A_3 ($C_T = 0.026$) reduced significantly as compared with panel C_3 ($C_T = 0.051$).

The trend of shift in spatio-temporal location of $\phi = 0$ and corresponding change in instantaneous forces with respect to panels B_3 and C_3 is illustrated for panel B_1 and C_6 configurations as depicted in figures 9(a) and 9(b), respectively. The effective stiffness of panel B_1 ($\Pi = 0.08$) is smaller than panel B_3 ($\Pi = 0.18$) and therefore it can been seen that the spatio-temporal location of the inflection for panel B_1 has moved towards the right on the time axis as compared with panel B_3. Whereas, with a higher effective stiffness of panel C_6 ($\Pi = 0.25$), the spatio-temporal location of the inflection has moved towards the left on the time axis as compared with panel C_3 ($\Pi = 0.06$). The instantaneous peak F_x on the negative side was reduced with an increase in the flexibility for panel B_1, however, the mean C_T is found to have remained nearly the same for both B_1 and B_3 configurations (figure 2). In the case of panel C_6, significant increases in the instantaneous peak F_x and mean C_T are observed when compared with C_3 (figures 2 and 8c).

Figures 10(a) and 10(b) depict the instantaneous force data for panels B_6 and C_8 whose effective stiffness value is higher than 0.6. Owing to higher stiffness, the trend of phase lag is found to be very different than the previous configurations. There is only a small increment in ϕ from $0°$ to $10–15°$ range and the spatio-temporal location of $\phi = 0$
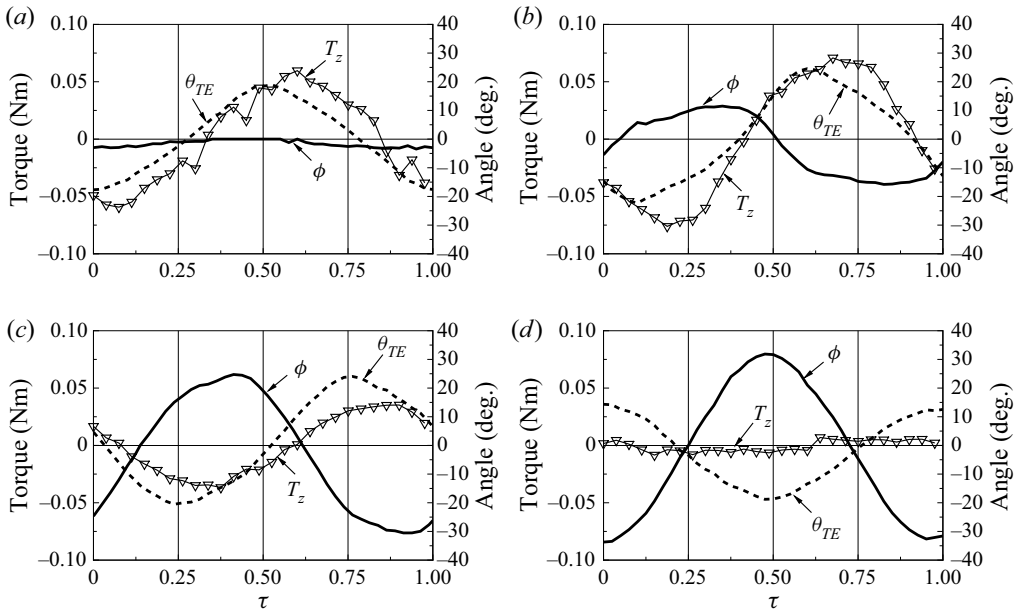
Figure 11. Instantaneous torque (T_{hyd}) experienced by the panel plotted against a non-dimensional cycle time. Torque (T_{hyd}), $\triangledown$; phase lag (ϕ), solid line; TE angle, dashed line; for (a) panel A_3 ($\Pi = 3.27$) (b) panel B_3 ($\Pi = 0.18$) (c) panel C_3 ($\Pi = 0.06$) (d) panel D_3 ($\Pi = 0.001$) having same aspect ratio of 0.625.

observed to be at the stroke extremes indicating that panel B_6 and C_8 are almost behaving like a rigid panel configuration. However, the high-speed imaging of panel B_6 and C_8 revealed that in these configurations the panel, instead of lagging behind the pointer, overtook it, and reached the extreme of the stroke before it. Towards the end of the stroke ($\tau = 0.9$) where the pointer loses its speed, the panel, which was lagging behind the pointer, gets a forward push (panel gets bent slightly) from the ensuing fluid having a higher Y-momentum. Hence, at the beginning of the new stroke, owing to the fluid resistance, the panel lags behind the pointer.

In the case of a pure plunging motion, a normal force is generated as a reaction to the plunging (Kang *et al.* 2011). In the present case of a pure pitching motion, the panel rotation and fluid resistance cause the generation of a hydrodynamic torque T_{hyd} and therefore it is also important to understand the time-evolution of T_{hyd} in a cycle. Figures 11(a) to 11(d) depict the time-evolution of T_{hyd} for panel A_3, B_3, C_3 and D_3, respectively. The trend of T_{hyd} variation is similar to that for F_y. We can say that the generation of lateral force (F_y) is directly correlated to T_{hyd} and Π. For panel A_3, peak T_{hyd} is present at the stroke reversals ($\tau = 0$, 0.5 and 1). There is a shift in peak T_{hyd} on the time axis for panel B_3 and C_3 and its spatio-temporal location correspond to where the phase lag is maximum (figures 11b and 11c). The change in sign of T_{hyd} prior to $\phi = 0$ for panel B_3 and C_3 indicates a bending of the panel in the direction opposite to the direction of T_{hyd}. The generation of hydrodynamic torque for panel D_3 is found to be insignificant (figure 11d).

3.3. *Hydrodynamic torque, phase lag and flexural stiffness analysis*

Hitherto we have learned the evolution of the panel kinematics and dynamics over a non-dimensional cycle time. We also have seen from the kinematics that the phase lag
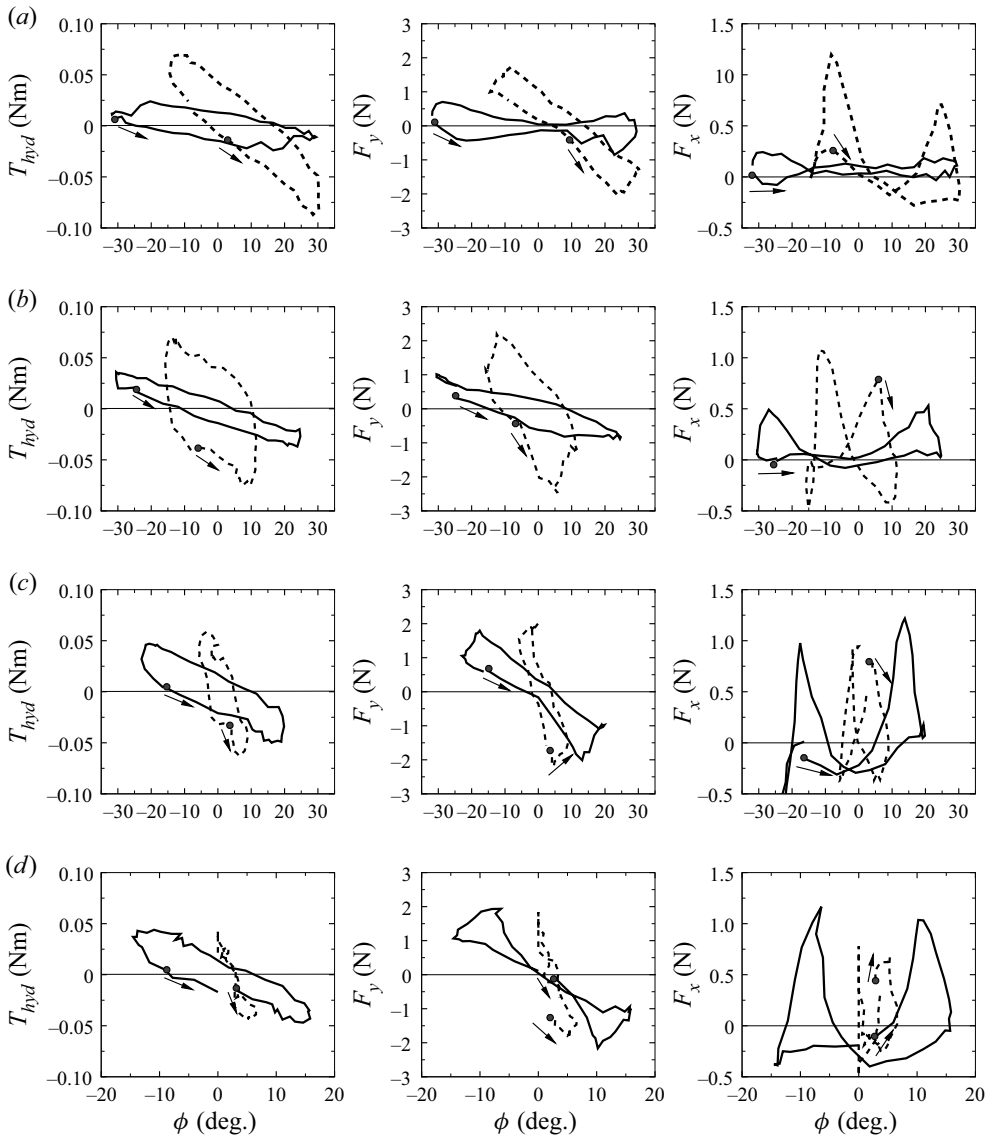
Figure 12. Variation of T_{hyd}, F_y and F_x as a function of ϕ for panel B (dashed line) and panel C (solid line) for aspect ratio (*a*) 0.44 ($\Pi_{B1} = 0.08$ and $\Pi_{C1} = 0.026$) (*b*) 0.625 ($\Pi_{B3} = 0.18$ and $\Pi_{C3} = 0.06$) (*c*) 1.1 ($\Pi_{B6} = 0.77$ and $\Pi_{C6} = 0.25$) and (*d*) 1.6 ($\Pi_{B8} = 1.92$ and $\Pi_{C8} = 0.62$). Filled circle and arrow show the beginning and direction of the cycle.

ϕ is closely associated with the panel deformation. Therefore for deep insight into the present FSI problem, it is essential to understand the phase-evolution of the hydrodynamic forces and torque. For this purpose, we have plotted T_{hyd}, F_y and F_x as a function of ϕ for panel B and C for four different aspect ratios shown in figures 12(*a*) to 12(*d*). An interesting trend of forces, and torque with phase lag for various aspect ratios has emerged. Firstly, the phase lag is higher for panel C than panel B for a given aspect ratio and with an increase in aspect ratio (figures 12*a* to 12*d*) the phase lag is reduced. The torque (plot shown in the first column in figures 12*a* to 12*d*) varies almost linearly until the lag becomes highest.

922 A13-16

At ϕ_{max}, on both sides of $\phi = 0$, the torque varies abruptly (kinky curve), and can be seen prominently in figures 12(*a*) to 12(*c*). For an aspect ratio of 1.6 (figure 12*d*) the phase-lag variation for panel B_8 shows that it is experiencing a large variation in torque for a small deflection (the torque phase-lag variation curve is almost vertical). For figures 12(*a*) to 12(*c*), however, the abrupt variation in T_{hyd} for a nearly constant lag ($\phi \approx \phi_{max}$) between two kinks suggests that the panel deflection has saturated. As ϕ begins to approach zero, the panel starts to unwind itself and subsequently comes to its original undeformed state where the lag becomes zero ($\phi = 0$). The trend of F_y (plot shown in the second column in figures 12*a* to 12*d*) is found to be similar to that for T_{hyd}. The torque/lateral force generation and panel deformation are directly related to the panel flexural stiffness, however, the relation between the longitudinal force (F_x) generation (about which we are concerned) and the flexural stiffness is difficult to understand, as is its trend with respect to the phase lag. The trend of F_x (plot shown in the third column in figures 12*a* to 12*d*) shows two peaks. With an increase in lag on either side of $\phi = 0$, the longitudinal force increases. However, unlike the trend of torque/lateral force variation, the longitudinal force reaches its peak, not at ϕ_{max}, but just before it and, additionally, F_x is found to become zero at ϕ_{max}. Recall figure 8, where the time gap between peak F_x and ϕ_{max} is considerable (depends on flexibility), this suggests that after reduction in longitudinal force, the torque continues to increase further before the panel begins to unwind itself.

We would like to emphasise the fact that this is the case of passive deformation. Daniel & Combes (2002) mentioned that it is possible to predict the instantaneous shape of a wing during flapping, for wings moving in air applications, using a theory of solid mechanics. However, for a high-density medium such as water, it is necessary to solve a complete set of FSI formulations in order to predict wing deformation. Even experimentally, it is rather difficult to establish the correlation between instantaneous panel deformation with both inertial–elastic and fluid-dynamic forces. There is a predominant effect of fluid-dynamic forces on both the panel bending and the hydrodynamic torque generation during pitching motion. However, we understand that panel flexural stiffness is the only factor that puts a limit on the highest deformation and so on the resulting torque experienced by the panel. Therefore we can say that both T_{hyd} and ϕ are 'in tune' with the panel flexural stiffness only at an instance where the panel deflection is highest (ϕ_{max}), and simple beam theory can be used only at the time instance of highest deformation of the panel. Thus there is a special significance to the maximum torque generation and the maximum deflection for a given panel flexural stiffness. Therefore we normalised the torque as

$$C_{Tq} = \frac{T_{hyd}}{0.5\rho_f U_t^2 bc^2}, \tag{3.3}$$

and took the ratio of C_{Tq} and ϕ both corresponding to the highest deflection where the longitudinal force F_x became zero, and analysed its trend with the effective flexural stiffness Π for various panel configurations. Figure 13(*a*) shows C_{Tq}/ϕ_{max} plotted as a function of Π and the second-order polynomial found to be the best curve-fit for the set of data points. Interestingly the slope (m) of this curve is $2T_{hyd}c(1 - v_p^2)/(\phi)(EI) = m$, which is analogous to the standard slope equation for a cantilever beam deflected owing to a moment at its free end $Ml/(\theta)(EI) = 1$, where M is the moment, l is the beam length and θ is the slope at beam's free end. The value of m is high (≈ 2.8) at lower values of Π and reduces with an increase of Π. The relation between ϕ_{max} and θ can be reduced further to $\theta = m\phi_{max}$. Thus, we can estimate θ and from it, the maximum deflection (δ_{max}) of the
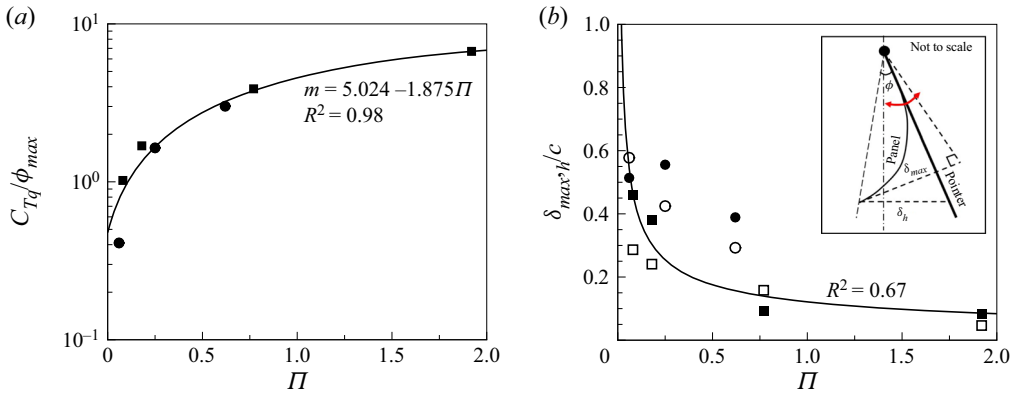
Figure 13. Variation of (a) C_{Tq}/ϕ_{max} and (b) $\delta_{max,h}/c$ as a function of Π. the symbols □ and ○ depict panel B and C configurations, respectively. Filled and empty symbols in figure 13(b) denote δ_{max} and δ_h, respectively. The schematic defining δ_{max} and δ_h is depicted in the inset of figure 13(b).

panel can be find out from the standard equation

$$\delta_{max} = \frac{Ml^2}{2EI}. \tag{3.4}$$

We then substitute $\theta = m\phi$ to replace $(Ml)/(EI)$ to get δ_{max} as

$$\delta_{max} = m\phi_{max}\frac{c}{2}. \tag{3.5}$$

Figure 13(b) shows the estimated maximum deflection of the panel as a function of Π. The lateral distance δ_h between the panel trailing edge and pointer, measured from the high-speed images is also shown in the plot. The deflection δ_h defined in the inset of figure 13(b) has been used to understand its trend with an increase in Π. Both estimated δ_{max} and measured δ_h were found to decrease with an increase in panel stiffness. Thus, our hypothesis of the resemblance of the torque-lag relation at the highest panel deflection using simple beam theory appears justified to a certain extent.

3.4. *Wake vortex characteristics*

In this section, we have presented the flow field around the panel obtained from the PIV measurements. In the present panel configurations, because the panel has a rotational motion about its leading edge we can say that only the trailing edge of the panel would generate and shed the vortex. The inception and development of TEV during pitching is represented by four phases and is shown in figures 14 to 17 for panels A_3, B_3 C_3 and D_3. We have shown the TEV development only for the pitching starting from the left extreme of the stroke. In all the figures the positions of the panel and the pointer have been shown in every phase for better visualisation of the results. In the case of rigid panel A_3, the inception of the TEV at the stroke reversal ($\tau = 0$) can be seen from the velocity vectors and iso-vorticity contours. In the absence of deformation, however, during stroke reversal the fluid particles following the panel motion have to lose their momentum in the lateral direction, and only those particles in the vicinity of the trailing edge were able to curl around its edge. We noted that the vortex formation is sluggish ($\tau = 0.12$ to 0.22) and the tangential velocity of the panel trailing edge is the same as
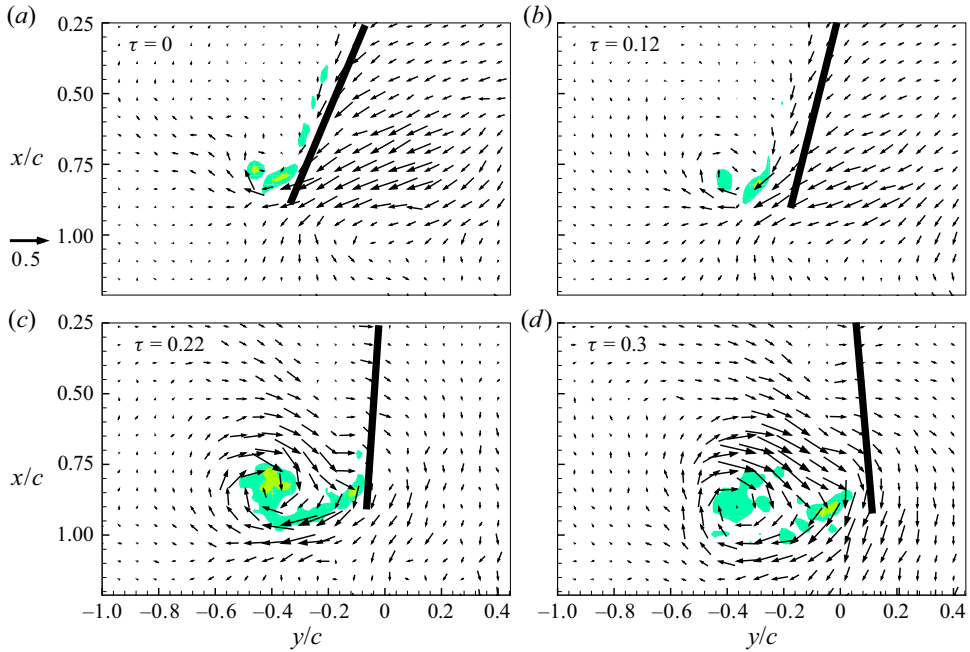
922 A13-18

Figure 14. Flow-field characteristics for panel A_3 are illustrated by the phase-averaged vorticity field superimposed with velocity vectors shown at different instances in a pitching cycle. Both the panel and pointer are pitching from left to right. Normalised vorticity contour levels shown are $\omega^* = 5, 10, 15, \ldots$.
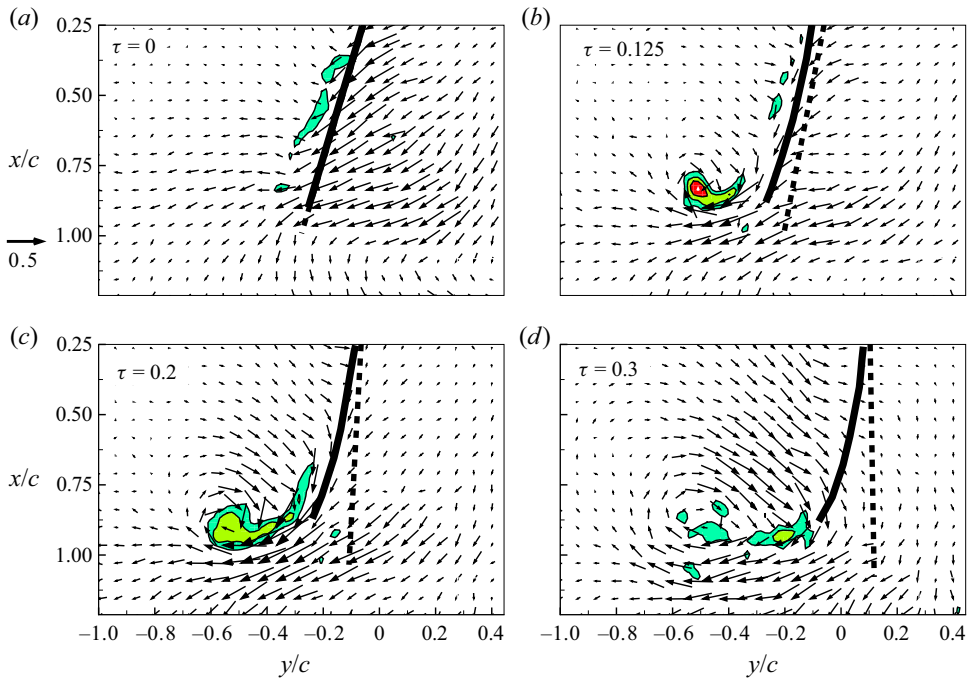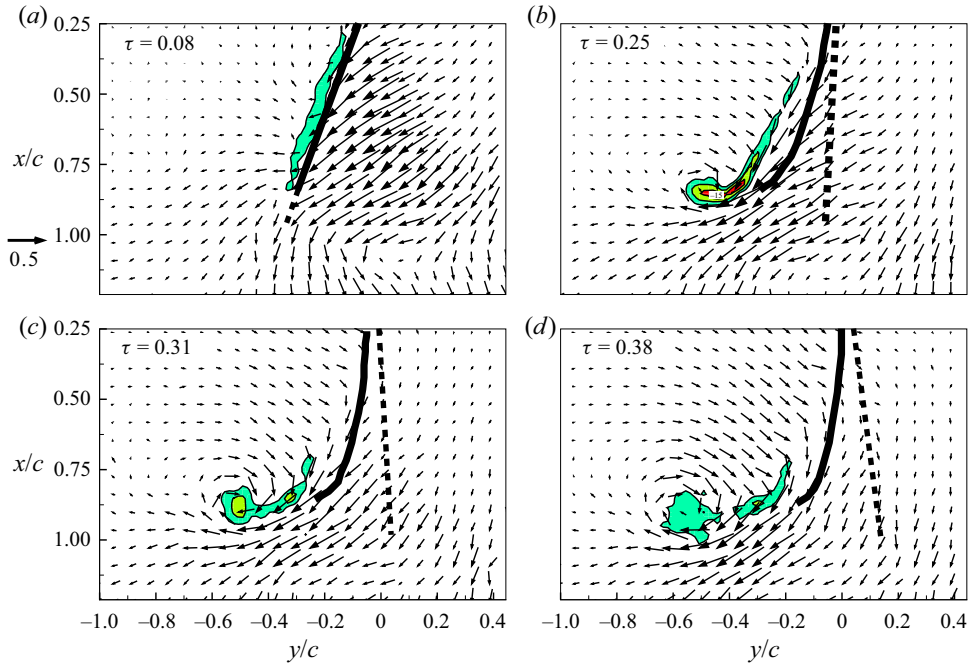

Figure 15. Flow-field characteristics for panel B_3 are illustrated by the phase-averaged vorticity field superimposed with velocity vectors shown at different instances in a pitching cycle. Both the panel and pointer are pitching from left to right. Normalised vorticity contour levels shown are $\omega^* = 5, 10, 15, \ldots$.
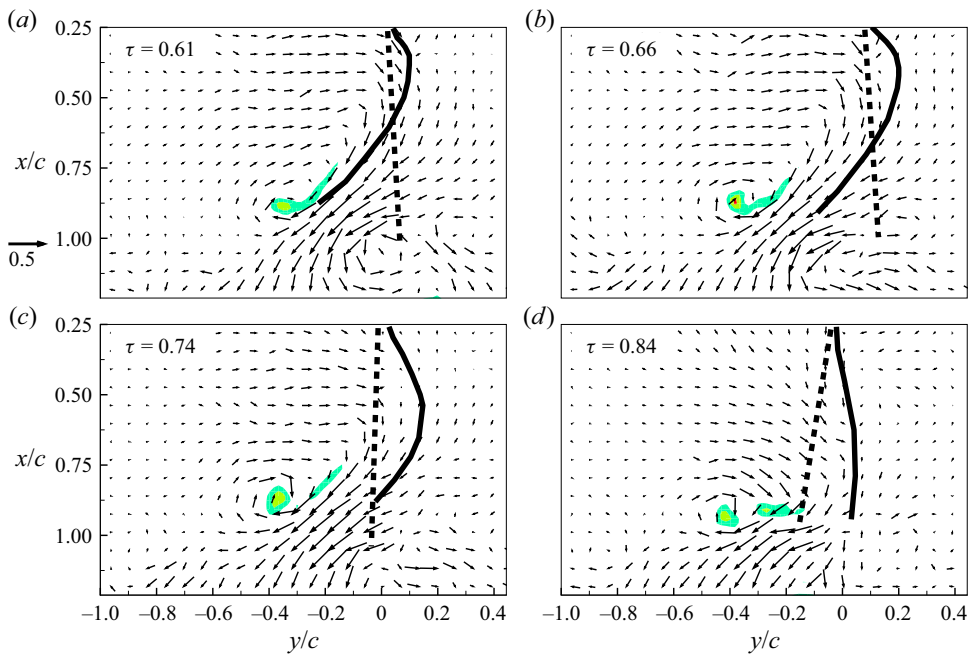
Figure 16. Flow-field characteristics for panel C_3 are illustrated by the phase-averaged vorticity field superimposed with velocity vectors shown at different instances in a pitching cycle. Both the panel and pointer are pitching from left to right. Normalised vorticity contour levels shown are $\omega^* = 5, 10, 15, \ldots$.

Figure 17. Flow-field characteristics for panel D_3 are illustrated by the phase-averaged vorticity field superimposed with velocity vectors shown at different instances in a pitching cycle. The panel is pitching from left to right and pointer is pitching from right to left. Normalised vorticity contour levels shown are $\omega^* = 5, 10, 15, \ldots$.

922 A13-20

the forcing function. The combined effect of sluggish TEV development and relatively faster panel speed resulted in the formation of a fully grown vortex away from the panel surface (Percin *et al.* 2011) which diminished the positive effect of the TEV on the thrust generation. For the moderately flexible panels B_3 and C_3 (figures 15 and 16), at the panel inflection, the momentum gained by the fluid in the lateral direction pushed the panel causing its elastic deformation. Owing to the elastic deformation, the velocity vectors are seen to align themselves along the deflected contour of the panel, also negotiating the trailing edge with little loss of momentum in the lateral direction. With the flexible panel configurations, the vortex is found to have sustained for a longer duration of time as the panel motion is reduced during the stroke reversal (figures 15 and 16) when compared with the rigid panel motion. For panels B_3 and C_3 we can see that as the panel continues to deform during stroke reversal, the fluid constantly fed the vorticity to the vortex through a filament connecting the trailing edge and the core of the vortex. We can observe that as the panel rotates after stroke reversal, this filament gets stretched and the vortex grows in size without much movement of its core. We can also see that at the highest deformation ϕ_{max} ($\tau = 0.3$ for panel B_3 and $\tau = 0.38$ for panel C_3), the vortex has diffused or detached from the trailing edge. The flow field for panel D_3 is found to be different than for panel B_3 and C_3 configurations (figure 17). We can see for panel D_3 that there is a delay in the TEV formation. For the left-to-right movement of the panel, the inception of TEV is found to take place only in the second half-cycle of the pitching ($\tau = 0.61$). Please recall the result discussed in the kinematics of pitching section where, the motion of the trailing edge of panel D_3 and the pointer were nearly out of phase owing to the higher-order deformation of the panel. Moreover, the formed TEV is found to get detached from the trailing edge only in a short interval of time ($\tau = 0.61$ to 0.66), and its size is also found to be smaller when compared with the other moderately flexible panel configurations. Factors such as delay in vortex formation, small size and early detachment from the panel surface and generation of weak lateral and longitudinal force are the consequence of the higher-order elastic deformation owing to lower effective stiffness of panel D_3. For all panel configurations, we did not observe the formation of reverse Kármán vortex street. Shinde & Arakeri (2014) mentioned the smearing of the vortex for a rigid two-dimensional foil. The effective stiffness for all the present panel configurations is found to be much higher (the flexural stiffness of panel D_3 is two order magnitude higher) when compared with the two-dimensional flexible foil cases studied by Shinde & Arakeri (2014). Thus relatively higher panel stiffness might have caused the faster dissipation of the vortex.

The evolution of the vortex from its inception to dissipation was found to have matched precisely with the time, and phase-evolution of the thrust generation stipulates a strong association between them. Thus, the panel flexibility allows fluid to deform its shape such that it directs the high momentum fluid towards a longitudinal axis without much loss, and thus enhancement in the longitudinal force is attributed to the moderate elastic deformation when compared with the rigid panel configuration.

4. Conclusion

This paper has comprehensively elucidated the kinematics and dynamics of the pitching motion of various flexible panel configurations in a quiescent fluid. Four panels having different thicknesses, further categorised into ten different aspect ratios were considered in the study. The panel surface area was kept constant for all the aspect ratios. Thus, the variations in chord and span of the panel were used as parameters to vary the flexural

stiffness of the panel (excluding thickness variation). The simultaneous measurements of forces F_x, F_y and torque T_{hyd} along with the leading-edge angle θ_{LE} were performed during a pure pitching motion of the various panel configurations. A high-speed imaging technique was used to estimate the trailing-edge angle θ_{TE} of the panel. PIV measurements were also performed and the time-evolution of the TEV from its inception to a fully grown size was described. In general, a variation of coefficient of thrust C_T based on time-averaged thrust is found to increase with aspect ratio, and for a given aspect ratio a large variation in C_T with the various panel configurations suggested a strong dependency of C_T on the panel effective stiffness Π. The collapse of the C_T data as a function of Π is obtained after eliminating the aspect ratio effect and a generic correlation between C_T and Π is established. With this $C_T - \Pi$ correlation, it is now possible to maximise the thrust generation simply by maintaining the effective stiffness value for the panel within a certain range. Highly flexible panel D configurations exhibited very much less thrust generation owing to higher-order elastic deformation.

The time-evolution of leading-edge angle, trailing-edge angle, and phase lag have revealed interesting features of the panel motion. Owing to flexibility, the panel could not follow the forcing function given to the pitching shaft because its trailing edge lagged behind the leading edge owing to elastic deformation. Particularly at stroke reversals, the panel motion is found to be reduced owing to flexibility. The phase lag ϕ variation in a cycle is used to describe the essential characteristics of panel deformation such as $\phi = 0$ and $\phi = \phi_{max}$ represent the inflection and maximum elastic deformation of the panel, respectively. The time-evolution of forces showed that the generation of a longitudinal force begins at the panel inflection irrespective of the panel flexibility. An increase in the panel flexibility was found to generate a higher longitudinal force (indirectly depends on the panel flexibility) for a longer duration owing to a reduced panel motion that improved the time-averaged thrust over a cycle compared with the rigid panel. From phase-averaged PIV data, we found that the inflection $\phi = 0$ and maximum deformation $\phi = \phi_{max}$ are the positions where the vortex is found to grow and dissipate, respectively. We have precisely pointed out experimentally, perhaps for the first time, that the inception of panel deformation, vortex formation and longitudinal force generation belong to an identical time in a pitching cycle.

The analysis of phase-evolution of the forces and torque further assisted in bringing out the relation of hydrodynamic torque T_{hyd} and maximum phase lag ϕ_{max} with the effective flexural stiffness Π. We realised the fact that for a given pitching frequency and amplitude, the flexural stiffness of the panel has a profound effect on both the hydrodynamic torque generation and the highest elastic deformation. In addition, the spatio-temporal location of the panel inflection, stroke reversal and highest deformation is found to be governed by the stiffness of the panel. We understood that the generation of longitudinal force is only an outcome of the previously mentioned factors, and that it is difficult to establish a direct correlation between the instantaneous longitudinal force generation and the flexural stiffness of the panel. In other words, the flexibility has a secondary effect on longitudinal force generation. However, we successfully attempted to establish a direct correlation between the effective flexural stiffness Π and T_{hyd}/ϕ_{max} ratio. This relation resembles the standard equation for a slope of a cantilever beam deflection owing to a moment acting at its free end. Based on the $T_{hyd} - \phi_{max}$ correlation, we estimated the maximum deflection δ_{max} of the various panel configurations. The result of a decrease of estimated δ_{max} with an increase in the stiffness of the panel is corroborated well by the measured lateral gap

δ_h between the trailing edge and the pointer for the highest phase lag ϕ_{max}, indicating that the correlation between T_{hyd}/ϕ_{max} and Π holds well.

Finally, we have highlighted the mechanism of instantaneous force generation, its time- and phase-evolution owing to pitching motion in the case of flexible panels. We believe that this time- and phase-evolution of the forces will help in understanding better the flying and swimming capabilities of all the relevant species in nature. In addition, based on this understanding, one can think of utilising smart material-based actuators where the panel flexibility can be varied dynamically in a pitching cycle to maximise the performance of the flexible propulsor for underwater vehicle applications.

Author ORCIDs.

Ⓓ Parag Deshpande https://orcid.org/0000-0003-2719-3837;

Ⓓ Abhijeet Vishwasrao https://orcid.org/0000-0002-5118-7245.

REFERENCES

ANDERSON, J.M., STREITLIEN, K., BARRETT, D.S. & TRIANTAFYLLOU, H.S. 1998 Oscillating foils of high propulsive efficiency. *J. Fluid Mech.* **360** (5), 41–72.

BUCHHOLZ, J.H.J. & SMITS, A.J. 2008 The wake structure and thrust performance of a rigid low-aspect-ratio pitching panel. *J. Fluid Mech.* **613**, 331–365.

COLEMAN, D., GAKHAR, K., BENEDICT, M., TRAN, J. & SIROH, J. 2018 Aeromechanics analysis of a hummingbird-like flapping wing in hover. *J. Aircraft* **55** (6), 2282–2297.

COMBES, S.A. & DANIEL, T.L. 2001 Shape, flapping and flexion: wing and fin design for forward flight. *J. Expl Biol.* **204**, 2073–2085.

COMBES, S.A. & DANIEL, T.L. 2003 Flexural stiffness in insect wings I. Scaling and the influence of wing venation. *J. Expl Biol.* **206** (17), 2979–2987.

DANIEL, T.L. & COMBES, S.A. 2002 Flexible wings and fins: bending by inertial or fluid-dynamic forces. *Integr. Comput. Biol.* **42**, 1044–1049.

DAVID, J.M., GOVARDHAN, R.N. & ARAKERI, J.H. 2017 Thrust generation from pitching foils with flexible trailing edge flaps. *J. Fluid Mech.* **828**, 70–103.

DESHPANDE, P.J. & MODANI, A. 2019 Experimental investigation of fluid-structure interaction in a bird-like flapping wing. *J. Fluids Struct.* **91**, 102712.

DEWEY, P.A., BOSCHITSCH, B.M., MOORED, K.W., STONE, H.A. & SMITS, A.J. 2013 Scaling laws for the thrust production of flexible pitching panels. *J. Fluid Mech.* **732**, 29–46.

GREEN, M.A. & SMITS, A.J. 2008 Effects of three-dimensionality on thrust production by a pitching panel. *J. Fluid Mech.* **615**, 211–220.

HEATHCOTE, S. & GURSUL, I. 2007 Flexible flapping airfoil propulsion at low Reynolds numbers. *AIAA J.* **45** (5), 1066–1079.

HEATHCOTE, S., WANG, Z. & GURSUL, I. 2008 Effect of spanwise flexibility on flapping wing propulsion. *J. Fluids Struct.* **24**, 183–199.

KANG, C.-K., AONO, H., CESNIK, C.E.S. & SHYY, W. 2011 Effects of flexibility on the aerodynamic performance of flapping wings. *J. Fluid Mech.* **689**, 32–74.

LAUDER, G.V., ANDERSON, E.J., TANGORRA, J. & MADDEN, P.G.A. 2007 Fish biorobotics: kinematics and hydrodynamics of self-propulsion. *J. Expl Biol.* **210**, 2767–2780.

MARAIS, C., WESFREID, J.E. & GODOY-DIANA, R. 2012 Stabilizing effect of flexibility in the wake of a flapping foil. *J. Fluid Mech.* **710**, 659–669.

MASSEY, K., FLICK, A. & JADHAV, G. 2009 Force measurements and flow visualization for a flexible flapping wing mechanism. *47th AIAA Aerospace Sciences Meeting Including The New Horizons Forum and Aerospace Exposition*, AIAA Paper 2009-877.

MOORE, N.M.J. 2014 Analytical results on the role of flexibility in flapping propulsion. *J. Fluid Mech.* **757**, 599–612.

PERCIN, M., HU, Y., VAN OUDHEUSDEN, B.W., REMES, B. & SCARANO, F. 2011 Wing flexibility effects in clap-and-fling. *Intl J. Micro Air Veh.* **3** (4), 217–227.

QUINN, D.B., LAUDER, G.V. & SMITS, A.J. 2014 Scaling the propulsive performance of heaving flexible panels. *J. Fluid Mech.* **738**, 250–267.

QUINN, D.B., LAUDER, G.V. & SMITS, A.J. 2015 Maximizing the efficiency of a flexible propulsor using experimental optimization. *J. Fluid Mech.* **767**, 430–448.

RAMANANARIVO, S., GODOY-DIANA, R. & THIRIA, B. 2011 Rather than resonance, flapping wing flyers may play on aerodynamics to improve performance. *Proc. Natl Acad. Sci. USA* **108**, 5964–5969.

RAMANANARIVO, S., GODOY-DIANA, R. & THIRIA, B. 2012 Passive elastic mechanism to mimic fish-muscle action in anguilliform swimming. *J. Fluid Mech.* **710**, 659–669.

SANE, S.P. & DICKINSON, M.H. 2002 The aerodynamic effects of wing rotation and a revised quasi-steady model of flapping flight. *J. Expl Biol.* **205** (8), 1087–1096.

SHINDE, S.Y. & ARAKERI, J.H. 2014 Flexibility in flapping foil suppresses meandering of induced jet in absence of free stream. *J. Fluid Mech.* **757**, 231–250.

SHKARAYEV, S. & RAJEEV, K. 2014 Instantaneous forces in locust flapping wings. In *Proceedings of 32nd AIAA Applied Aerodynamics Conference*. AIAA.

SMITS, A.J. 2019 Undulatory and oscillatory swimming. *J. Fluid Mech.* **874**, P1.

VANELLA, M., FITZGERALD, T., PREIDIKMAN, S., BALARA, E. & BALACHANDRAN, B. 2009 Influence of flexibility on the aerodynamic performance of a hovering wing. *J. Expl Biol.* **212**, 95–105.

WU, P., STANFORD, B.K., SAILLSTROM, J., UKEILEY, L. & IFJU, P.G. 2011 Structural dynamics and aerodynamics measurements of biologically inspired flexible flapping wings. *Bioinspir. Biomim.* **6**, 016009.

WU, X., ZHANG, X., TIAN, X., LI, X. & LU, W. 2020 A review on fluid dynamics of flapping foils. *Ocean Engng* **195**, 106712.

ZHANG, J., LIU, N.-S. & LU, X.-Y. 2010 Locomotion of a passively flapping flat plate. *J. Fluid Mech.* **659** (5), 43–68.

ZHAO, L., HUANG, Q., DENG, X. & SANE, S.P. 2010 Aerodynamic effects of flexibility in flapping wings. *J. R. Soc. Interface* **7**, 485–497.

ZHU, R., WANG, J., LEWIS, G., ZHU, J., DONG, H., BART-SMITH, H., WAINWRIGHT, D. & LAUDER, G. 2017 Propulsive performance of pitching panels with bio-inspired passive directional flexibility. *47th AIAA Fluid Dynamics Conference*, AIAA Paper 2017-3980.